Accepted Manuscript

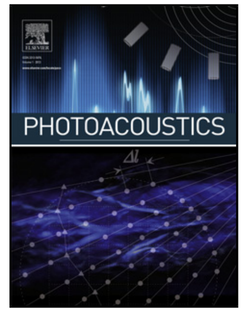

Title: Characterization of Lens Based Photoacoustic Imaging System

Author: Kalloor Joseph Francis Bhargava Chinni Sumohana S. Channappayya Rajalakshmi Pachamuthu Vikram S. Dogra Navalgund Rao

PII:	S2213-5979(17)30021-6
DOI:	https://doi.org/doi:10.1016/j.pacs.2017.09.003
Reference:	PACS 82

To appear in:

Received date:	4-5-2017
Revised date:	14-9-2017
Accepted date:	18-9-2017

Please cite this article as: Kalloor Joseph Francis, Bhargava Chinni, Sumohana S. Channappayya, Rajalakshmi Pachamuthu, Vikram S. Dogra, Navalgund Rao, Characterization of Lens Based Photoacoustic Imaging System, *<![CDATA[Photoacoustics]]>* (2017), https://doi.org/10.1016/j.pacs.2017.09.003

Characterization of Lens Based Photoacoustic Imaging System

Kalloor Joseph Francis[a,1,], Bhargava Chinni[b], Sumohana S. Channappayya[a], Rajalakshmi Pachamuthu[a], Vikram S. Dogra[b], Navalgund Rao[c,2,]

[a]*Department of Electrical Engineering, Indian Institute of Technology Hyderabad, India - 502285.*
[b]*Department of Imaging Sciences, University of Rochester Medical Center, 601 Elmwood Ave, Rochester, NY, USA, 14642.*
[c]*Chester F. Carlson Center for Imaging Science, Rochester Institute of Technology,54 Lomb Memorial Drive, Rochester, NY, USA, 14623.*

Abstract

Some of the challenges in translating photoacoustic (PA) imaging to clinical applications includes limited view of the target tissue, low signal to noise ratio and the high cost of developing real-time systems. Acoustic lens based PA imaging systems, also known as PA cameras are a potential alternative to conventional imaging systems in these scenarios. The 3D focusing action of lens enables real-time C-Scan imaging with a 2D transducer array. In this paper, we model the underlying physics in a PA camera in the mathematical framework of an imaging system and derive a closed form expression for the point spread function (PSF). Experimental verification follows including the details on how to design and fabricate the lens inexpensively. The system PSF is evaluated over a 3D volume that can be imaged by this PA camera. Its utility is demonstrated by imaging phantom and an *ex vivo* human prostate tissue sample.

Keywords: Acoustic lens, Photoacoustic camera, Point Spread Function,

Email addresses: `ee14resch12001@iith.ac.in` (Kalloor Joseph Francis), `narpci@cis.rit.edu` (Navalgund Rao)
[1]Corresponding author,
Supported by the US Fulbright program.
[2]Principal corresponding author
This work was supported by grant from NIBIB, NIH through Grant No. 1R15EB019726-01. We greatly acknowledge Lang memorial foundation for providing financial support for the laser.

Resolution, *ex vivo* imaging.

1. Introduction

The photoacoustic (PA) phenomenon employs pulsed laser light to induce thermoelastic pressure increase in the tissue absorbers, which in turn leads to the generation of ultrasound (US) waves. PA imaging techniques focus on efficient ways to measure these US waves and form an image representative of the optical absorption profile of the tissue. This unique combination of light and sound brings together the high contrast capability of optical imaging and the high resolution of US imaging [1]. The intrinsic optical contrast of tissue molecule at specific wavelengths in the near infrared window enables PA imaging to be a potential modality in clinical applications like the early cancer diagnosis, metabolism imaging, etc. [2].

Conventional reconstruction algorithms use triangulation on multiple sensor observations to localize tissue absorbers [3]. Typically, given the US propagation model and measurement from multiple sensors, the profile of the initial pressure can be reconstructed. These methods require measurements on a closed surface surrounding the target volume and for this reason are effective in imaging small animals and *ex vivo* tissue samples. However, in clinical studies, US measurement on such a closed surface is nearly impossible. For example in thyroid and prostate imaging, a 360^0 view of the target tissue is hindered by other body parts resulting in a limited set of views. Robust reconstruction of tissue absorption profile from these limited measurements is an ongoing challenge for PA imaging [4, 5, 6]. Additionally, these reconstruction algorithms are computationally complex, and real-time imaging requires expensive and dedicated hardware [7]. In this paper, we present the design, fabrication and use of an acoustic lens based imaging system which we call a PA camera, as a possible alternative to the digital reconstruction based methods mentioned above. The key difference is that in the latter, spatial and temporal sampling of the PA signal occurs before the reconstruction while in the former, reconstruction, or more correctly focusing, occurs in the continuous space-time domain and the PA signal is sampled subsequently. Like in an optical camera, an acoustic lens is used to simultaneously focus PA signal from different points in a 3D volume. The lens performs the major task of focusing the pressure profile from an object plane to the corresponding imaging plane, thus eliminating the need for reconstruction algorithms. A PA camera is ideally suited for real-time C-scan imaging with the availability of a 2D sensor array in the imaging plane. However, a B-scan image can also be formed using a linear US transducer array, without the need for reconstruction algorithms.

Early works on sound focusing using acoustic lens can be found in [8, 9], where the authors studied focal length and gain with an acoustic lens. A more extensive theoretical and experimental study on the pressure gain with a biconcave lens can be found in [10]. With the wide use of acoustic lens attached to single element US transducers, the sound field and focusing action have become a well understood technique. However, time consuming point by point scanning is required with such a set-up to acquire C-scan or B-scan image data [11]. The imaging system we describe in this paper is different in that the lens is placed in between the object plane and the imaging plane, and a multi-element US sensor array acquires image data simultaneously at multiple pixel locations. In 2006, He et al. [12] used an acoustic lens for the first time in PA imaging. Other works from the group also include the peak holding circuit for real-time PA imaging [13] and the introduction of $4F$ imaging system [14, 15, 16]. A low-cost method using 3D printing technology to manufacture acoustic lenses and a preliminary characterization was conducted by Rao et al. in 2008 [17]. Along with the use of $4F$ imaging system, the group developed a scanning probe, known as PA camera [18]. This technique has proved to be a cost-effective alternative to the conventional PA imaging system with several advancements on the clinical side, including *ex vivo* studies [19] and system designs for *in vivo* imaging [20]. All these systems are designed to time-gate the acoustic signal to image an object plane at $2F$ distance from the lens. An attempt to image multiple depths is presented in [21] with limited success in phantom studies. Several important aspects lacking in the literature include a rigorous system characterization of such a PA imaging camera, resolution analysis of the system and the identification of limiting factors. It is also not clear how to specify the design parameters of an acoustic lens and a transducer to obtain a required resolution. In this work, we intend to bridge the gap between PA camera design and applications and also to open up possibilities of post-processing.

A theoretical model for the PA camera is presented in Section 2. We analyze wave propagation through a thin acoustic lens and present an expression for the pressure detected by the transducers. The proposed model is very flexible in that it allows for the computation of theoretical PSF for any camera design. We also propose a new PA signal model mimicking Gabor wavelets for a finite size source in this section. In Section 3, we present a PA camera design and a detailed specification of the PSF and tissue imaging experiments. In Section 4, a comparison of the theoretical and experimental PSFs is presented along with a study of changes in the PSF at off-axis and on-axis locations. We also demonstrate *ex vivo* prostate tissue imaging as an application of this system. We discuss the advantages and limitations of the proposed theoretical model and the system in Section 5.

2. Theory

In this section we derive the PSF of the acoustic lens, combining the wave propagation with the thin lens model. A separable theoretical axial and lateral PSF for the lens-based system is presented.

Acoustic lens-based imaging system: In acoustics, a biconcave surface is used as a converging lens if the index of refraction of the lens material is higher than the surrounding medium. The design of a spherical biconcave lens with focal length F and diameter 2ρ is considered here. To achieve a unit magnification we consider the object plane and imaging plane at a distance of $2F$ on either side of the lens as in Fig. 1. The unit magnification was chosen to eliminate the need for scaling the obtained image in this study. However, the lens allows

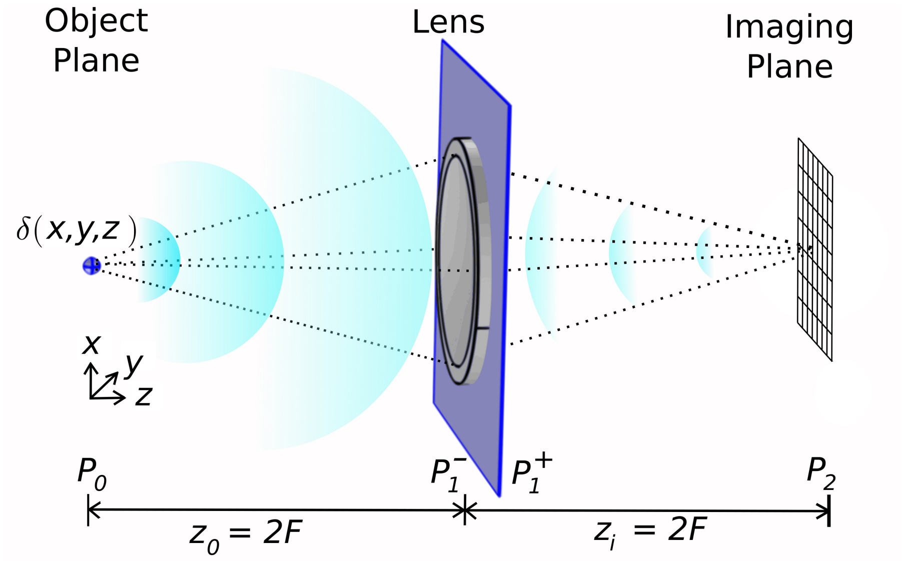

Figure 1: Acoustic lens system with $4F$ geometry. z_o is the distance between object plane and lens, z_i is the distance between lens and imaging plane. P_0 is the object plane, P_1^- plane anterior to the lens, P_1^+ plane posterior to the lens and P_2 is the imaging plane. F is the focal length of acoustic lens.

for a different magnification as well. Laser exposure (not shown) excites a short US pressure profile at the object plane P_0. US waves from the object plane propagate in water to the anterior plane at P_1^-. The lens introduces a phase change to the wavefront, focusing and forming an image at the image plane P_2.

Acoustic lens action: Consider an US point source $\delta(x, y, z)$ at the origin. Let us consider the wave generated by the point source having an envelop signal $a(t)$ modulated with a sinusoid $e^{-i\omega_0 t}$. The source at origin can be defined as,

$$P_0(x, y, z, t) = \delta(x, y, z)a(t)e^{-i\omega_0 t}, \tag{1}$$

where t is time, $\omega_0 = 2\pi f_0$, and f_0 is the modulation frequency. US waves propagating from the source in a homogeneous medium satisfies the wave equation,

$$\bigtriangledown^2 p(r,t) - \frac{1}{c^2}\frac{\partial^2}{\partial t^2}p(r,t) = 0, \tag{2}$$

where $r = \sqrt{x^2+y^2+z^2}$, c is the sound speed and $p(r,t)$ is the impulse response of the medium. We can write the impulse response of the medium as the solution to the wave equation,

$$p(r,t) = \frac{1}{r}\delta(t - r/c). \tag{3}$$

This is the spherical wavefront generated by a pressure pulse at a distance r over time t. To find the wavefront at the anterior plane P_1^-, the source can be convolved with the impulse response of the medium, $P_1^-(r,t) = P_0(r,t) * p(r,t)$ giving,

$$P_1^-(r,t) = \frac{1}{r}a(t - r/c)e^{-i\omega_0(t-r/c)} \tag{4}$$

where $(*)$ is convolution operation. Substituting for object distance $r = z_o$ and applying Fresnel approximation [22],

$$P_1^-(x,y,z,t) = \frac{1}{2F}a(t - 2F/c)e^{-i\omega_0 t}e^{ik_0 z_o}e^{i\frac{k_0}{2z_o}(x^2+y^2)}, \tag{5}$$

where $k_0 = \omega_0/c$. A thin spherical biconcave acoustic lens with edge thickness Δ_0 introduces a phase shift to the wavefront given by (derived in Appendix A),

$$\Phi(x,y) = e^{ik_0\Delta_0}e^{-ik_0\frac{x^2+y^2}{2F}}. \tag{6}$$

Any possible attenuation of the wave in the lens material has been neglected for the sake of mathematical simplicity. Additionally, the lens can only focus wavefronts within its aperture of diameter 2ρ. Hence the aperture function is given by,

$$\Psi(x,y) = \begin{cases} 1, & \text{if } x^2+y^2 \le \rho^2 \\ 0, & \text{otherwise.} \end{cases} \tag{7}$$

The total lens transfer function is the product of phase and aperture function. The wavefront at P_1^+ is given by $P_1^+(x,y,z,t) = P_1^-(x,y,z,t)\Phi(x,y)\Psi(x,y)$. Substituting and rearranging,

$$P_1^+(x,y,z,t) = \frac{1}{2F}a(t - 2F/c)e^{-i\omega_0 t}e^{ik_0(z_o+\Delta_0)}\Psi(x,y)e^{i\frac{k_0}{2}\left(\frac{1}{z_o}-\frac{1}{F}\right)(x^2+y^2)}. \tag{8}$$

The wavefront at imaging plane P_2 is the convolution of wavefront at P_1^+ with the impulse response of the medium from lens to detector plane $h(x, y, z, t)$, $P_2(x, y, z, t) = P_1^+(x, y, z, t) * h(x, y, z, t)$. Consider a change of variable from (x, y) for the convolution term to (u, v) for P_1^+ and applying Fresnel approximation,

$$P_2(x, y, z, t) = \frac{1}{z_i} \int\int P_1^+(u, v, z, t - z_i/c) e^{\frac{ik_0}{2z_i}\left[(x-u)^2+(y-v)^2\right]} dudv, \quad (9)$$

where z_i the distance between the lens and the imaging plane. Substituting for P_1^+,

$$P_2(x, y, z, t) = \mathbb{A}(t)\mathbb{P}(z)\mathbb{Q}(x, y) \int\int \Psi(u, v) e^{\frac{-ik}{z_i}(ux+vy)} e^{\frac{ik}{2}(u^2+v^2)\left[\frac{1}{z_o}+\frac{1}{z_i}-\frac{1}{F}\right]} dudv \quad (10)$$

where,

$$\mathbb{A}(t) = \frac{1}{(2F)^2} a(t - 4F/c) e^{-i\omega_0 t},$$
$$\mathbb{P}(z) = e^{ik_0 z}\Big|_{z=z_i+z_o+\Delta_0},$$
$$\mathbb{Q}(x, y) = e^{\frac{ik_0}{2z_i}(x^2+y^2)}.$$

$\mathbb{A}(t)$ is the time domain signal with an amplitude scaling and time shift. Typically, to form a PA image from a finite object, only an envelope of time gated PA signal is required. Thus, the phase information of the incoming wavefront is relatively insignificant. $\mathbb{P}(z)$ is the phase shift introduced by the system corresponding to the total length $z_o + z_i + \Delta_0$. Since it is a constant phase, it can be neglected. $\mathbb{Q}(x, y, z)$ is the quadratic phase term in-plane P_2, which does not affect the intensity (PSF) and thus can also be neglected [22]. As a special case, when $z_i = z_o = 2F$, $\frac{1}{z_o} + \frac{1}{z_i} - \frac{1}{F} = 0$, the equation reduces to,

$$h(x, y, t) = \frac{1}{(2F)^2} a(t - 4F/c) e^{-i\omega_0 t} \iint_{u^2+v^2 \le \rho^2} e^{\frac{-ik}{2F}(ux+vy)} dudv. \quad (11)$$

This integral has a closed form solution. Let α_m be the angle subtended by the edge of the lens with the lens axis. For $\rho \ll 2F$, we can use the small angle approximation for $\sin(\alpha_m) \approx \alpha_m$. Replacing $r' = \sqrt{x^2 + y^2}$, the radial distance from the lens axis, the PSF can be expressed as,

$$\begin{aligned} h_L(r', t) &= \left[a(t - 4F/c)e^{-i\omega_0 t}\right]\left[\alpha_m^2 \, \mathrm{jinc}(k\alpha_m r')\right], \\ &= h_L(t)h_L(r'). \end{aligned} \tag{12}$$

where $\mathrm{jinc}(x) = J_1(x)/x$, and J_1 is the Bessel function of the first kind. The PSF at this point is a product of a time dependent term $h_L(t)$ and a circularly symmetric spatial term $h_L(r')$. Although Eq. (11) can be computed for any arbitrary lens diameter value, the closed form solution using the small angle approximation is valid only for $\alpha_m \leq 14^0$.

Using an US sensor element of a finite size introduces a spatial smoothing on the PSF. This can be represented by a convolution with a 2D rectangular function $g_T(x, y)$. Similarly, the finite bandwidth of the transducer modifies the time dependent signal via a convolution with transducer impulse response $g_T(t)$. The final system PSF is given by

$$\begin{aligned} h_F(r', t) &= [h_L(r')h_L(t)] * [g_T(x, y)g_T(t)], \\ &= [h_L(r') * g_T(x, y)] [h_L(t) * g_T(t)]. \end{aligned} \tag{13}$$

Similar to US imaging, two separate resolution metrics, namely axial and lateral, can be defined by Eq. (13) for the PSF. The full width at half maximum (FWHM) of the spatial part $h_L(r') * g_T(x, y)$ represents the lateral resolution of the imaging system in the (x, y) plane. The FWHM of the envelope detected temporal part $h_L(t) * g_T(t)$ determines the axial resolution along the z-axis with t and z related via $ct = z$. Spatial and temporal sampling in this imaging system takes place after this point in the imaging chain. If we assume that the focused image in the (x, y) plane at $z = 4F$ is sampled using a 1D or 2D array, with a uniform sampling interval of $\Delta x = \Delta y = \Delta s$. Then the system will have a spatial Nyquist frequency of $1/(2\Delta s)$. Similarly, the temporal part will have a temporal Nyquist frequency $2f_s$, given that digital A-line data sampling rate is f_s.

PA signal model: As we are interested in validating the model experimentally, and an ideal point source is impossible in practice, a source of finite size is considered. A spherical source with uniform absorption results in an **N** shaped PA signal [23]. However, for many practical cases, a Gaussian absorption profile is appropriate. Let $A(r) = A_0 e^{-\frac{1}{2}\left(\frac{r}{R_e}\right)^2}$, where A_0 is the peak value of Gaussian determined by the absorption and laser intensity. R_e is the $1/\sqrt{e}$ radius of the absorber. Hoelen et al. [24] proposed a **N** shaped pulse modulated with the Gaussian profile as PA signal. We found that a Gabor wavelet can almost exactly fit this model (shown in Appendix B). We also have the flexibility from Gabor wavelet formulation to have scales and translations. We define the PA signal from a spherical absorber as a sinusoid modulated by a Gaussian function defined by,

$$P(r,t) = P_{max} e^{-\frac{1}{2}\left[\frac{t-\tau}{\tau_{pp}/2}\right]^2} e^{-i\omega_0(t-\tau)}, \tag{14}$$

where P_{max} is the peak amplitude of PA signal proportional to A_0, $\omega_0 = 2\pi f_0$ and $f_0 = \frac{1}{2\tau_{pp}}$, r is the distance from source center to detector, $\tau = r/c$ and $\tau_{pp} = 2R_e/c_s$ with c_s as sound speed inside absorber. The width of the Gaussian and the frequency of the sinusoid can be defined in terms of source diameter. The source model has been used in deriving the final PSF in Eq. (12), with $a(t) = P_{max} e^{-\frac{1}{2}\left[\frac{t-\tau}{\tau_{pp}/2}\right]^2}$.

3. Methods

In this section, the design of the bi-concave lens for PA camera is presented along with the specification of the imaging system. We also present details on the PSF experiment and tissue imaging.

Lens design: An ideal lens material should, (i) have the acoustic impedance close to that of propagation medium (water) to maximize transmission of acoustic energy, and (ii) have as large an index of refraction (defined as the ratio of longitudinal US speed in water to that in the lens material) as possible. For fast prototyping and impedance matching with water, we chose the plastic material DSM18420, with sound speed $c_2 = 2590$ m/s and the density is $\rho_2 = 884.17$

kg/m^3 [25] . With this material and water as medium 90%, of the incident energy is estimated to be transmitted through both surfaces of the lens using perpendicular incident transmission energy equation [26]. A practical advantage of the material is that it is used in 3D printing technology which eliminates the need for expensive lens making procedure. The next design parameter is the focal length and the radius of curvature. For potential *in vivo* imaging of thyroid and breast, the diameter and focal length were arbitrarily picked to design a compact handheld cylindrical probe no more than 16 cm in length and less than 4 cm in diameter. Thus we chose the radius of curvature of the lens to be 33.5 mm on both side of the lens ($R_1 = R_2 = R$) and diameter as 32 mm. Using lens makers formula [8],

$$\frac{1}{F} = (1-\mu)\left[\frac{1}{R_1} + \frac{1}{R_2}\right], \tag{15}$$

where $\mu = c_1/c_2$ is refractive index, with c_1 and c_2 being sound speed in water (1500 m/s) and lens material (2590 m/s) respectively. The focal length of the lens was calculated to be 39.8 mm. Similar to optics, the design parameters were tested for a single wavelength using optical lens design software, OSLO [27]. The wavelength used was 0.32 mm in water corresponding to our 5 MHz transducer center frequency. For fast in-house prototyping and flexibility in developing an embedded lens in a probe, the manufacturing was carried out with a 3D printing technology. A 3D rapid prototype printer employing stereolithography technology at a fine resolution of 0.254 mm - 0.381 mm was used to print the lens and post processed with pattern fitting prime finish. In the lens manufacturing, the center thickness is selected to be 0.5 mm, considering the 3D printer resolution. Compared to theory where a zero center thickness is assumed the signal can be time shifted due to finite lens thickness. We have estimated this time shift to be 0.2 μs and have compensated to match with the theoretical model. However, the nature of the signal remains unchanged as the time shift caused by the finite thickness is smaller than the PA pulse width. The attenuation in the lens material was measured to be 0.5 dB/mm/MHz. The lens being biconcave, its thickness varies from approximately 0.5 mm in the center to 5 mm at the edges and 1.6 mm at the half way point. The attenuation, therefore, is expected to have a spatially varying apodization effect on the incident wave front. The implications of this are taken up later in the discussion section.

Experimental setup for lens evaluation: Lens PSF experiments were done in a water tank. The US transducer array and the point source were placed at $2F$ distance on opposite sides of the lens as in Fig. 1. The source and detector were aligned first, and fine distance measurement of $4F$ was made by measuring the time of flight from the laser trigger to the peak signal received. Using a vernier caliper, the lens was placed at $2F$ distance from both source and transducer and finely adjusted to achieve maximum pressure at the imaging plane. The laser beam was incident on the point source aligned along the lens axis. A pulsed laser (EKSPLA Inc NT-352A), tuned at 790 nm wavelength with a pulse duration of 5 ns and pulse repetition rate of 10 Hz was used as the light source. The laser exposure was kept at ≈ 13 mJ/cm^2, which is less than the ANSI limit 40 mJ/cm^2 at 790nm [28, 29]. Acoustic signals generated from the target were focused by the lens to the imaging plane. A 16 element linear transducer array from Olympus NDT with a pitch of 0.5 mm, element size of 0.5 mm $\times$ 1 mm and center frequency of 5 MHz with 55% bandwidth was used for detecting the acoustic waves. When the object had a larger area than the transducer active area (8 mm in linear and 1 mm in elevation), a C-scan was performed to acquire the data. The obtained PA signals were amplified using a custom made 16 channel amplification stage with 50 dB gain. The A-line signals were digitized using National Instruments PXI-5105 with a sampling rate of 60 MHz. The envelope detection of A-line signals was computed by applying the Hilbert transform and then observing the absolute value of the signal. These envelope detected A-line signals were placed side-by-side to form a B-scan image. From the standpoint of ideal spatial delta function defined in Eq. (1), the target diameter should be as small as possible. Unfortunately, very small size PA target will generate a very high dominant frequency signal [23], that may fall outside the bandwidth of our transducer. With this trade-off in mind, a 0.2 mm diameter graphite ball was used as the point source for PSF experiments. 3D motion stages (Zaber Technologies Inc.) were used to position the point source, lens and transducer at different off-axis and depth points. A US absorbing baffle was placed to prevent direct waves outside the lens diameter from reaching the transducer.

Setup for phantom and tissue imaging: Imaging experiments on phantom and *ex vivo* tissue sample were performed with a probe having a cylindrical body with lens fitted in the middle and US array at one end, in a $4F$ imaging geometry [30, 31, 32]. The whole probe with the lens was 3D printed eliminating tedious lens and transducer alignment requirement. One end of the probe was water sealed using an acoustically transparent polymethylpentene sheet. This allows us to couple the probe to the tissue or phantom using a coupling gel. We used a phantom with graphite structures embedded in US gel pad. The phantom size used for imaging was of 20 mm $\times$ 25 mm $\times$ 2.5 mm. Three point targets of 0.7 mm diameter at 0.25 mm, 1.3 mm and 2 mm depth respectively from the phantom surface and four line targets of length 3 mm and 0.7 mm diameter were embedded inside the gel phantom as shown in Fig. 5a. The phantom to be imaged was placed with its surface perpendicular to the z axis and its center at $2F$ distance from the lens, and the data was collected in a C-scan format using stepper motor stage [30, 32]. 2D C-scan images were generated pertaining to different depths by time gating the envelope detected A-line signals. The 3D PA image was formed by stacking the C-scan images. For phantom imaging, graphite absorbers were used and hence the laser illumination was set to 790 nm. Institutional Review Boards approval was obtained for this study. Written informed consent was obtained from the patient undergoing prostatectomy for biopsy confirmed prostate cancer. To detect malignant region in the tissue i.e., the region with high hemoglobin concentration due to growing blood vessels, we used a wavelength of 800 nm for the laser. With a fiber bundle of 8 mm diameter, approximatly ≈ 13 mJ/cm^2 of energy was delivered on the object which is less than the ANSI limit of 40 mJ/cm^2 at 790 nm and 800 nm [29]. With a reflective light delivery the handheld probe can be used for *in vivo* thyroid and breast imaging as well.

4. Results

According to Eq. (13), the PSF is three dimensional in nature. Assuming circular symmetry in the (x, y) plane, we measured two-dimensional (2D) slices (B-scan) of the PSF by placing a linear array of US transducer along the x axis. C-scan images of tissue depicting constant depth slices can also be generated by scanning the camera in the y direction followed by time gating the A-line signals at each pixel. To characterize the system, we have extracted several quality metrics of the experimentally measured 2D PSF. Axial and lateral profiles in the best focal plane and its variation for different depth planes and off-axis points are presented.

Comparison with theoretical predictions: For the $4F$ geometry, thin lens approximation would predict the best focal plane to be at $2F$ distance from the lens. Experimentally, based on the smallest size of the PSF and its peak value, we found the best focal plane to be only 3% off, at $2F + 2.5$ mm. Fig. 2a shows three normalized A-line PA signals for comparison. The black dashed line, labeled ideal, is the predicted PA time signal at the 0.2 mm diameter spherical source, as calculated from Eq. (14). In red is the theoretical PA signal given by Eq. (13), for an on-axis ($x = y = 0$) US transducer element. Note that for the temporal part, this also includes modifications imposed by the finite size of US sensor element and its finite bandwidth filtering. In blue is the experimentally measured PA signal at the center element of the linear transducer array. Fig. 2c shows the spectrum of theoretical and experimental signals in Fig. 2a. Envelope detected A-lines of these two signals is shown in Fig. 2b as a function of $z = ct$. For analysis purpose, axial Modulation Transfer Function (MTF) defined as the magnitude part of the Fourier transform of envelope detected A-line signal, is shown in Fig. 2d.

2D PSF images were generated by placing envelope detected A-lines side by side. In Fig. 4a column 4 shows the 2D PSF in the best focal plane for on-axis point source. Note that the horizontal 1D profile taken at the peak location of this PSF represents its axial profile and is identical to the blue line shown in

Fig. 2b. Similarly the 1D vertical profile of this PSF shown in Fig. 2e in blue represents the lateral profile. Shown in red in Fig. 2e is the theoretical lateral profile in the x direction calculated from Eq. (13). Parameters used were the same as those in the experiments, namely lens diameter $2\rho = 32$ mm, $2F = 79.6$ mm, transducer array element size is 0.5 mm $\times$ 1 mm and the dominant frequency of the finite bandwidth transducer $f_o = 5$ MHz. The two lateral MTFs corresponding to the two lateral profiles are shown in Fig. 2e. In spite of the approximations involved in the theory, the qualitative agreement is good. Quantitatively, the axial Full Width at Half Maximum (FWHM) was found to be 0.3475 mm and 0.3499 mm respectively for theory and experiments. Temporal sampling at 60 MHz results in a Nyquist frequency of 30 MHz and spatial Nyquist frequency in the axial direction of 20 cycles/mm. The lateral FWHM along the x-axis was found to be 1.54 mm for theory and 1.6 mm for the experiment. Similarly, the lateral FWHM along the y-axis was estimated to be 1.65 mm, but we did not make any measurement in the y direction. Given the spatial pitch of 0.5 mm in our linear array, the system lateral Nyquist frequency is 1 cycle/mm, as shown in MTF plot of Fig. 2e. Clearly, from the axial and lateral MTF plots, most of the dominant frequencies in the image are below the corresponding Nyquist frequencies, indicating that we have minimized aliasing in our system for the PA signals generated by a 0.2 mm point source. Factors that set the limits on resolution of this system are discussed later.

PSF at Different Depth Planes and Off-axis Points: While the experimental PSF is optimum for the on-axis point source in the plane at $2F$ distance from the lens, it is expected to degrade for planes that are closer or farther away along the z-axis, as well as for off-axis points along the x-axis. Due to the approximations, the theory we have presented cannot be used to predict these changes. Therefore we have experimentally determined multiple PSFs by placing the point source at different on-axis and off-axis distances. Fig. 3a shows the PSF for different on-axis source locations and Fig. 4a for off-axis locations

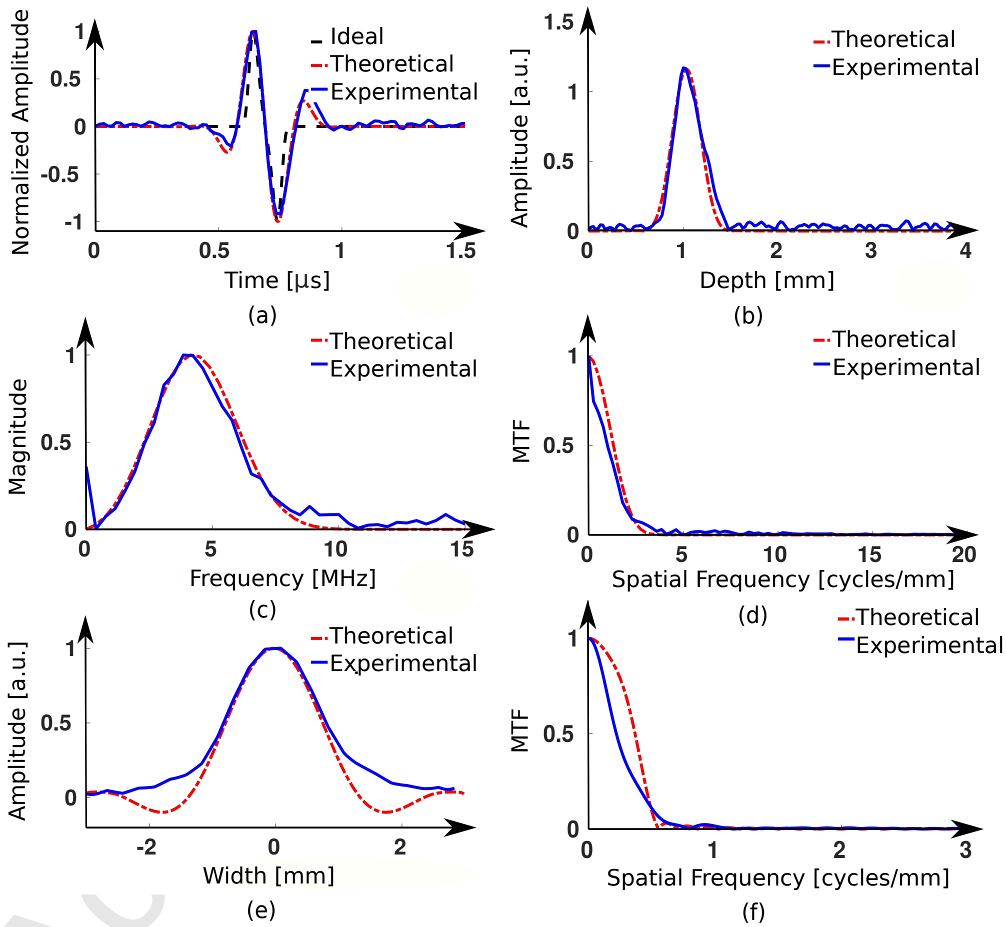

Figure 2: (a) A-line PA signal of center element, (b) Envelope detected A-line, (c) Spectrum of PA signal in (a), (d) Axial MTF, (e) Lateral PSF (f) Lateral MTF.

in the focal plane at $z = 2F$. In Fig. 3a, seven different PSFs are shown from left to right as the point source is placed receptively at distances $2F - 9$ mm, $2F - 6$ mm, $2F - 3$ mm, $2F$, $2F + 3$ mm, $2F + 6$ mm, and $2F + 9$ mm from the lens. Similarly, Fig. 4a shows seven PSFs for the point source placed in the focal plane at $2F$ respectively at off-axis distances -3 mm, -2 mm, -1 mm, 0 mm, 1 mm, 2 mm and 3 mm.

Qualitatively, we observed that PSF changes were minor as a function of off-axis distance, but were significant and measurable as a function of on-axis distance for different depth planes. To map the changes in the PSF in more detail, multiple PSFs were measured at 21 different depth planes, ranging in object distance from $2F - 1$ cm to $2F + 1$ cm, in steps of 1 mm. The image plane was fixed at a distance of $2F$ from the lens and the 16 element transducer array with a pitch of 0.5 mm was staggered during data acquisition to effectively reduce the pitch to 0.25 mm. Only for the $2F$ plane, 9 different off-axis, PSFs were measured distances along x-axis ranging from -2 mm to $+2$ mm.

To study these variations, we extracted three parameters from each PSF; (i) Axial-FWHM (ii) Lateral-FWHM and (iii) Normalized peak value. Fig. 4b shows the Axial-FWHM, Lateral-FWHM and peak variation for off-axis source locations. The Axial-FWHM of PSF is fairly constant around 0.35 mm, and Lateral-FWHM is bounded in 1.6 mm - 2.3 mm. The peak value decrease is insignificant, less than 3% for 2 mm off-axis point, indicating that in reality there is probably a larger field of view than what our data indicates. Fig. 3b shows parameter variation as a function of axial distance z or equivalently for different depth planes. The axial resolution is unaffected with depth, maintaining a value of 0.35 mm. The lateral resolution shows an asymmetry, maintaining a value of 1.6 mm for planes further away than $2F$ but for planes closer than $2F$, it gradually degrades to 4 mm due to defocusing effect of the lens. The peak value also decreases with increasing distance from the $2F$ plane on either side but remains above the 50% mark for the entire 2 cm range. The peak value is shifted from $2F$ planes and is located at $2F + 2.5$ mm plane as observed earlier. We may arbitrarily define the depth of field of this system as the range of z

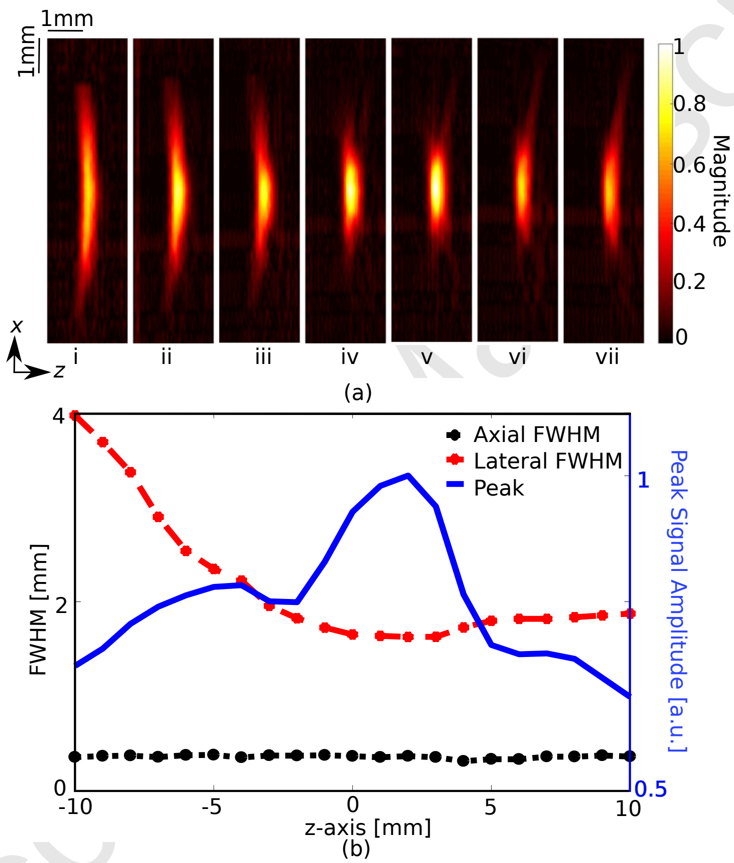

Figure 3: (a) PSF at 7 on-axis (z-axis) locations: from left to right at $2F - 9$ mm to $2F + 9$ mm with 3 mm increment. (b) PSF Lateral FWHM, Axial FWHM and normalized peak value for different z-axis location of the point source.

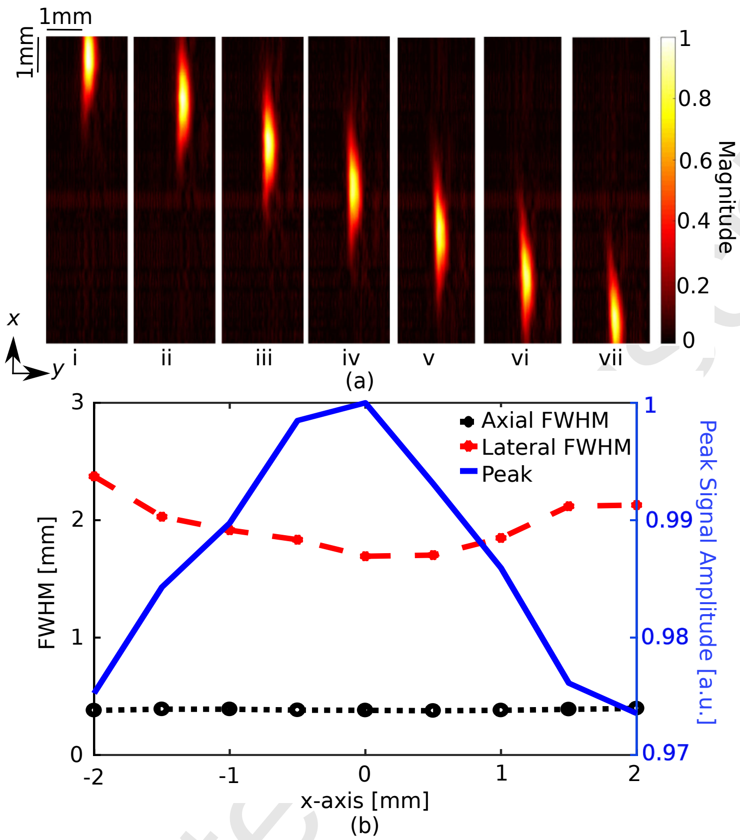

Figure 4: (a) PSF at 7 off-axis (x-axis) locations ranging from -3 mm to $+3$ mm at 1 mm increment (b) PSF Lateral FWHM, Axial FWHM and normalized peak value for different x-axis location of the point source.

values where the lateral FWHM does not degrade more than 50% of its best value. From Fig. 3b, the depth of field is around 18 mm about the best focal plane.

3D Phantom Imaging: Fig. 5a shows the phantom used in the experiment, with four line targets and three point target at different depths. The line targets are not perfectly aligned in a plane and are used to mark the boundary of the phantom. Arrows of different colors are marked on the phantom to point to the target PA sources. Fig. 5b shows the Maximum Intensity Projection (MIP) computed long the depth direction that combines all the objects for a 2D visualization. All the target absorbers in the phantom are visible in the image. Fig. 5 c, d and e represent C-scan slices in the volumetric PA image at 0.25 mm, 1.3 mm and 2 mm depths respectively. The target truncation artifact is due to sensitivity variation from the left end to the right end in the sensor array. All the line targets are visible in the MIP profile in Fig. 5b only because they were not necessarily coplanar with any of the point targets. The spread in PA image for line targets are due to defocus effect for different depths.

3D tissue imaging: Fig. 6a shows the photograph of a human prostate tissue sample that approximately covered 2 cm $\times$ 4 cm area and was less than 5 mm thick. This sample was placed in the $2F$ plane with its thickness aligned along the lens or the z-axis. The linear array covered a distance of 1 cm along the x-axis, and the scanning step size in the y direction was 1 mm. With a laser of 10 Hz pulse repetition frequency, it took 2 minutes to acquire 3D focused data set for this size sample. Fig. 6b shows a histology cross-section of the top tissue surface shown in Fig. 6a. The pathologist has marked a region in red within which malignant tissue was found under microscopic examination. The malignant region generally has a growing microstructure of blood vessels. Consequently, a high PA signal is expected from this region. As the resolution of the system cannot resolve the blood vessels individually, only a blurred image within the malignant region can be detected using the system. Fig. 6c shows the C-Scan PA image (xy plane) of the tissue sample at $2F$ plane in Fig. 6a. The image shows a high PA signal intensity profile inside the malignant region. Two other cross sectional slices of 3D PA image in xz and yz plane cutting through the malignant region are shown in Fig. 6d and Fig. 6e respectively. High intensity PA signal inside the malignant region can be seen in both the slices. This demonstrates that we can focus and localize PA signals from absorbers in 3 dimensions with our technology without any need for 3D computerized tomography based reconstruction algorithms.

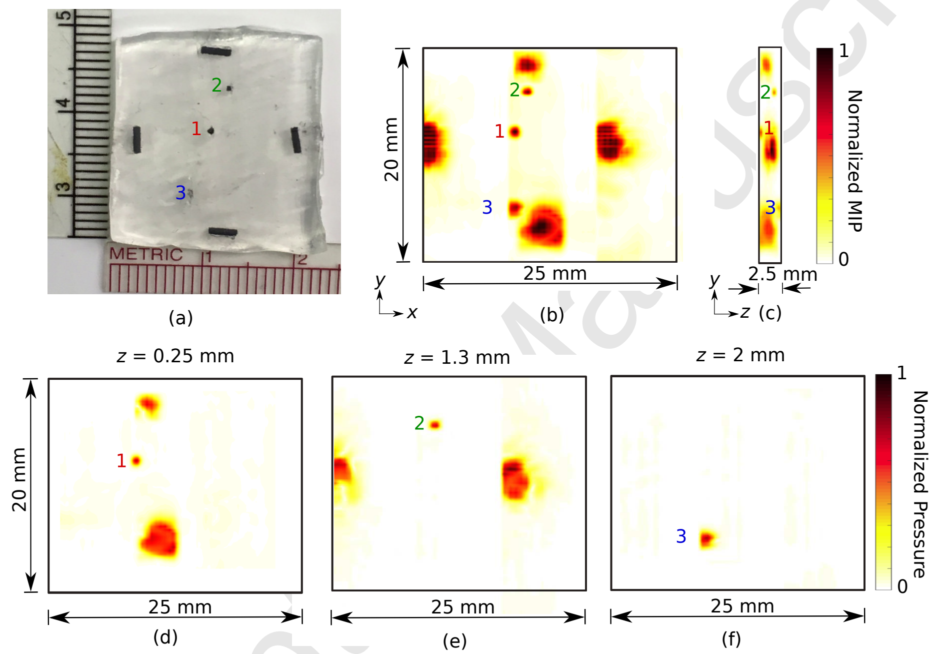

Figure 5: (a) Photograph of absorbers (three point absorbers and four line absorbers) embeded in ultrasound gel pad of 20 mm$\times$ 25 mm$\times$ 2.5 mm, (b) Maximum Intensity Projection (MIP) of the PA volume along the depth (z axis) showing intensity in xy plane. Numbers on the phantom photograph inticates point sources at different depth from the surface of the phantom, (c) MIP along x axis showing intensity image in yz plane, (d) PA image slice at 0.25 mm depth depicting point source 1, (e) PA image slice at 1.3 mm depth depicting point source 2, (f) PA image slice at 2 mm depth depicting point source 3.

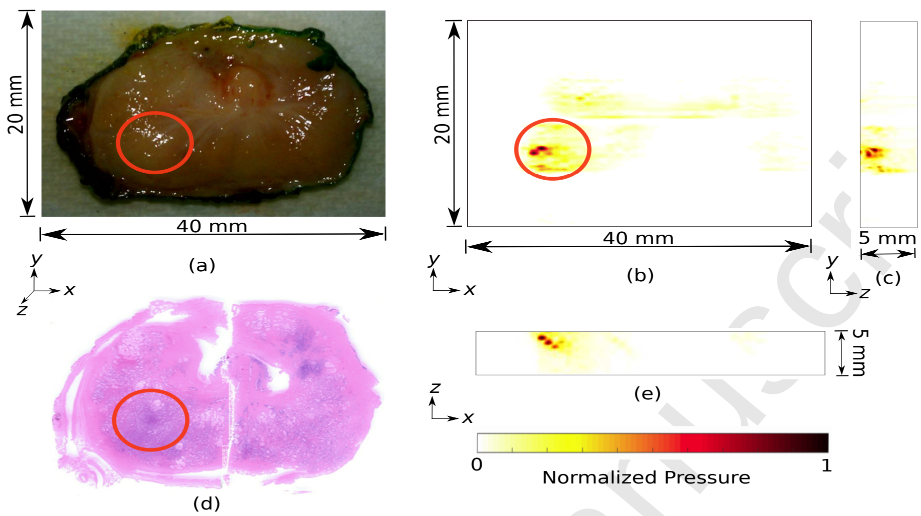

Figure 6: (a) Photograph of prostate tissue, (d) Histology image showing malignant region, (b) PA image C-Scan slice (xy plane) at $2F$ plane with the malignant region marked with red circle, (c) Cross sectional image (yz plane), through malignant region (e) Cross sectional image (xz plane) through the malignant region of interest.

5. Discussion

By using a quasi-monochromatic approximation, we were able to show theoretically that the on-axis system PSF in the focal plane is a product of two separable functions as in Eq. (13). First, there is the 2D spatial part $h_L(r')$ that represents lateral resolution in the focal plane. This function, being a convolution of a circularly symmetric lens $h_L(r')$ part with a rectangular transducer element area part $g(r')$, is itself not circularly symmetric. Then there is the 1D function of time or equivalently z, that represents the axial resolution. Our numerical calculations agree well with our experimental results, as evidenced by red and blue lines in Fig. 2. This allows us to draw some inferences regarding how the different physical parameters of the system affect the PSF. The lateral resolution increases with lens diameter and the dominant frequency of the PA signal but decreases with increasing focal length and area of the transducer element. The 0.5 dB/mm/MHz attenuation of the lens material has interesting consequences for the experimental PSF in the lateral direction. Because we neglect attenuation for the theory, the lens aperture function given by Eq. (7) has spatially constant transmission inside the lens but sharp discontinuity at the circular edge. This primarily results in jinc function behavior for the lateral part of the PSF as in Eq. (12). But for the experimental data, due to attenuation through varying thickness of the biconcave lens, we get in effect, a circularly symmetric transmission function that is close to one at the center but nonlinearly drops by 12 dB at the edges. This is similar to lens apodization through the coating in optics where the primary purpose is to reduce or eliminate the side lobes of the jinc function [33]. Data in Fig. 2 provides some evidence for this. In the theoretical lateral PSF, the first side lobe is clearly discernible from the central lobe but for the experimental lateral PSF, it is significantly diminished, at a cost of slightly increasing the foot of the central lobe. However, the two FWHM values remain comparable. This is a somewhat desirable consequence that comes at the expense of some overall loss in transmission. The axial resolution mainly increases with the bandwidth of the detected PA time signal and is relatively immune to other lens parameters [34]. Frequency dependence of attenuation of the lens material can have a low pass filtering effect on the spectrum of the PA time signal. If significant, the manifestations are observable on the down shift of the center frequency and a change in the bandwidth of the time signal [35]. In Fig. 2c we do not see any major difference between the theoretical and experimental spectrum after passing through the lens. We may conclude that for this lens material the thickness we have used has negligible impact on the signal spectrum up to 10 MHz. We were able to get the axial and lateral resolution of 0.3 mm and 1.6 mm respectively for our designed system.

In our system, the PSF was found to be spatially variant within a 1 cm $(x) \times 1$ cm $(y) \times 2$ cm (z) volume centered at $2F$ on-axis distance from the lens. Change in the axial resolution was insignificant, but the lateral resolution did vary degraded significantly outside the depth of field of 18 mm. Because of the approximations involved, the theory we have presented cannot be used to confirm or predict these changes in PSF. Qualitatively, it is well known that for single element focused US transducers, the best PSF is in the focal plane where Fraunhofer approximation holds, but the PSF degrades in a non-symmetrical fashion in front and back of the focal point as we move into regions where Fresnel approximation holds [26]. A similar phenomenon may be happening here, but we have not developed a detailed theory to account for it. As a minor point, it is interesting to note that the experimental focal point based peak value and smallest PSF size was not found at the geometrically predicted $2F$ distance but at $2F + 2.5$ mm. This deviation may be due to a small difference between the assumed curvature and the actual curvature of the manufactured lens.

To the best of our knowledge, the only C-scan based system on tomographic PA imaging we could find is the photoacoustic mammoscope system from the University of Twente [36] that can be compared to our system. Their system detects PA signal with a transducer matrix with a circular detecting area of 9 cm. It has stated average lateral resolution of 3.8 mm and axial resolution of 3.5 mm. The reason for lower resolution may partly be due to the lower frequency (1 MHz) of US transducer array and larger size of sensor element compared to our system. To illustrate the design flexibility of our system, we estimate that the lateral resolution in our system can change from 1.54 mm to 0.93 mm as we change diameter from 32 mm to 70 mm. Similarly, with a fixed diameter of 32 mm, the lateral resolution can change from 5.6 mm to 0.95 mm as the dominant frequency of the PA signal varies from 1 MHz to 10 MHz respectively.

In this lens characterization work, we have used a data acquisition system to acquire the PA signal. The hardware requirement is thus similar to tomographic PA imaging. However, C-scan imaging using a planar 2D array require significantly less hardware. The amplified and rectified PA signal can be time gated for one single arrival time and can be rendered for display. A feasibility study was already conducted for lens-based PA imaging by Wei et al. [16]. This eliminates the need for data acquisition at a high sampling rate and dedicated hardware for reconstruction algorithms. With this method, different depths inside the tissue can also be imaged by varying lens to transducer distance. Nonetheless, this advantage disappears if real-time 3D imaging is required. Even in 3D imaging, the cost required for a lens-based system can be less than that of a tomographic PA system.

A post processing aspect which we are working on is the residual refocusing procedure to increase the depth of field of our system. With this improved system, 3D volumetric data can be acquired in real-time but refocused later as a post processing step for improved diagnosis.

6. Conclusion

We have presented a theoretical model that predicts the PSF of a PA imaging camera. Experimental evaluation shows that the model accurately predicts the system performance in the focal plane. The theory helps us to understand how the lateral and axial resolution of the system depends on the relevant physical parameters such as lens diameter, focal length and transducer frequency response. A prototype PA camera system was designed, fabricated and its performance was experimentally evaluated. The designed system can focus PA signals generated from a small volume of an object when it is placed in the focal plane. The system capability was demonstrated, with 3D images of a phantom and a freshly excised *ex vivo* human prostate tissue sample. Acoustic lens-based technology may provide a cost effective alternative to tomographic PA imaging systems. We believe that our current work establishes a foundation upon which researchers can build wide-ranging innovations in lens design, such as zoom lens and wide angle lens for PA imaging applications.

References

[1] P. Beard, Biomedical photoacoustic imaging, Interface focus (2011) rsfs20110028.

[2] L. V. Wang, S. Hu, Photoacoustic tomography: in vivo imaging from organelles to organs, Science 335 (2012) 1458–1462.

[3] M. Xu, L. V. Wang, Universal back-projection algorithm for photoacoustic computed tomography, Physical Review E 71 (2005) 016706.

[4] Y. Xu, L. V. Wang, G. Ambartsoumian, P. Kuchment, Reconstructions in limited-view thermoacoustic tomography, Medical physics 31 (2004) 724–733.

[5] G. Paltauf, R. Nuster, M. Haltmeier, P. Burgholzer, Experimental evaluation of reconstruction algorithms for limited view photoacoustic tomography with line detectors, Inverse Problems 23 (2007) S81.

[6] C. Lutzweiler, D. Razansky, Optoacoustic imaging and tomography: reconstruction approaches and outstanding challenges in image performance and quantification, Sensors 13 (2013) 7345–7384.

[7] J. Kim, S. Park, Y. Jung, S. Chang, J. Park, Y. Zhang, J. F. Lovell, C. Kim, Programmable real-time clinical photoacoustic and ultrasound imaging system, Scientific reports 6 (2016).

[8] T. Tarnoczy, Sound focussing lenses and waveguides, Ultrasonics 3 (1965) 115–127.

[9] L. Rozenberg, Ultrasonic focusing radiators, in: Sources of High-Intensity Ultrasound, Springer, 1969, pp. 223–309.

[10] T. Nakamura, M. Hashimoto, K. Mori, T. Kamakura, T. Anada, Sound fields focused by a biconcave acoustic lens for normal and oblique incidence, in: Europe Oceans 2005, volume 1, IEEE, 2005, pp. 62–67.

[11] K. S. Valluru, B. K. Chinni, N. A. Rao, S. Bhatt, V. S. Dogra, Basics and clinical applications of photoacoustic imaging, Ultrasound Clinics 4 (2009) 403–429.

[12] Y. He, Z. Tang, Z. Chen, W. Wan, J. Li, A novel photoacoustic tomography based on a time-resolved technique and an acoustic lens imaging system, Physics in medicine and biology 51 (2006) 2671.

[13] H. Zhang, Z. Tang, Y. He, L. Guo, Two dimensional photoacoustic imaging based on an acoustic lens and the peak-hold technology, Review of scientific instruments 78 (2007) 064902.

[14] Z. Chen, Z. Tang, W. Wan, Photoacoustic tomography imaging based on a 4f acoustic lens imaging system, Optics express 15 (2007) 4966–4976.

[15] W. Wan, R. Liang, Z. Tang, Z. Chen, H. Zhang, Y. He, The imaging property of photoacoustic fourier imaging and tomography using an acoustic lens imaging system, Journal of applied physics 101 (2007) 063103.

[16] Y. Wei, Z. Tang, H. Zhang, Y. He, H. Liu, Photoacoustic tomography imaging using a 4f acoustic lens and peak-hold technology, Optics express 16 (2008) 5314–5319.

[17] N. A. Rao, D. Lai, S. Bhatt, S. C. Arnold, B. Chinni, V. S. Dogra, Acoustic lens characterization for ultrasound and photoacoustic c-scan imaging modalities, Ultrasound 1 (2008) 2.

[18] K. Valluru, B. Chinni, S. Bhatt, V. Dogra, N. Rao, D. Akata, Probe design for photoacoustic imaging of prostate, in: 2010 IEEE International Conference on Imaging Systems and Techniques, IEEE, 2010, pp. 121–124.

[19] V. S. Dogra, B. K. Chinni, K. S. Valluru, J. Moalem, E. J. Giampoli, K. Evans, N. A. Rao, Preliminary results of ex vivo multispectral photoacoustic imaging in the management of thyroid cancer, American Journal of Roentgenology 202 (2014) W552–W558.

[20] B. Chinni, Z. Han, N. Brown, P. Vallejo, T. Jacobs, W. Knox, V. Dogra, N. Rao, Multi-acoustic lens design methodology for a low cost c-scan photoacoustic imaging camera, in: SPIE BiOS, International Society for Optics and Photonics, 2016, pp. 97081Q–97081Q.

[21] X. Chen, Z. Tang, Y. He, H. Liu, Y. Wu, A simultaneous multiple-section photoacoustic imaging technique based on acoustic lens, Journal of Applied Physics 108 (2010) 073116.

[22] J. W. Goodman, Introduction to Fourier optics, Roberts and Company Publishers, 2005.

[23] I. G. Calasso, W. Craig, G. J. Diebold, Photoacoustic point source, Physical Review Letters 86 (2001) 3550.

[24] C. Hoelen, F. De Mul, A new theoretical approach to photoacoustic signal generation, The Journal of the Acoustical Society of America 106 (1999) 695–706.

[25] Look for protogen18420 datasheet, https://www.dsm.com/products/somos/en_US/products/offerings-somos-proto-gen.html (Last accessed: July 2017).

[26] T. L. Szabo, Diagnostic ultrasound imaging: inside out, Academic Press, 2004.

[27] J. Jeong, Oslo, Optical Science and Technology, Korea. http://lambdares.com/software_products/oslo (2006).

[28] J. Yao, A. A. Kaberniuk, L. Li, D. M. Shcherbakova, R. Zhang, L. Wang, G. Li, V. V. Verkhusha, L. V. Wang, Multiscale photoacoustic tomography using reversibly switchable bacterial phytochrome as a near-infrared photochromic probe, Nature methods 13 (2016) 67–73.

[29] American national standard for the safe use of lasers, American National Standards Institute. ANSIZ136. New York, NY: American National Standards Institute (2007).

[30] V. S. Dogra, B. K. Chinni, K. S. Valluru, J. V. Joseph, A. Ghazi, J. L. Yao, K. Evans, E. M. Messing, N. A. Rao, Multispectral photoacoustic imaging of prostate cancer: preliminary ex-vivo results, Journal of clinical imaging science 3 (2013).

[31] K. S. Valluru, B. K. Chinni, N. A. Rao, et al., Photoacoustic imaging: opening new frontiers in medical imaging, Journal of clinical imaging science 1 (2011) 24.

[32] K. S. Valluru, B. K. Chinni, N. A. Rao, S. Bhatt, V. S. Dogra, Development of a c-scan photoacoutsic imaging probe for prostate cancer detection, in: SPIE Medical Imaging, International Society for Optics and Photonics, 2011, pp. 79680C–79680C.

[33] W. H. Southwell, Using apodization functions to reduce sidelobes in rugate filters, Applied Optics 28 (1989) 5091–5094.

[34] M. Xu, L. V. Wang, Analytic explanation of spatial resolution related to bandwidth and detector aperture size in thermoacoustic or photoacoustic reconstruction, Physical Review E 67 (2003) 056605.

[35] Z. Klimonda, M. Postema, A. Nowicki, J. Litniewski, Tissue attenuation estimation by mean frequency downshift and bandwidth limitation, IEEE transactions on ultrasonics, ferroelectrics, and frequency control 63 (2016) 1107–1115.

[36] S. Manohar, A. Kharine, J. C. van Hespen, W. Steenbergen, T. G. van Leeuwen, The twente photoacoustic mammoscope: system overview and performance, Physics in medicine and biology 50 (2005) 2543.

7. Appendix A

Phase and pupil function of acoustic bi-concave lens: Consider an acoustic thin lens whose center thickness is zeros as in Fig. 7. The maximum thickness at the edge of the lens is Δ_0. R is the radius of curvature ($\Delta_0 \ll R$). $h = \sqrt{x^2 + y^2}$ is the perpendicular distance from central axis of lens. In this case, the radius of curvature on both sides of the lens is R. Consider the triangle ABC. The thickness of one side of the lens is,

$$\Delta_h = R - \sqrt{R^2 - (x^2 + y^2)} \tag{16}$$

Since $|x^2 + y^2|_{max} \ll R$, we can apply paraxial approximation using binomial expansion,

$$\Delta_h = \frac{x^2 + y^2}{2R}. \tag{17}$$

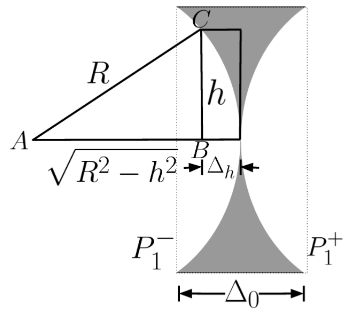

Figure 7: Thin lens with thickness Δ_h at a height h.

Thickness at any location in the lens (x, y) is $2\Delta_h = \frac{x^2+y^2}{R}$. In this study, water is taken as the medium. Path from P_1^- to P_1^+ can be written as path in water and path in lens,

$$\Delta_w(x, y) = \Delta_0 - \Delta(x, y), \tag{18}$$

and path in lens

$$\Delta_l(x, y) = \Delta(x, y). \tag{19}$$

Phase transform from P_1^- to P_1^+ can be expressed as,

$$\begin{aligned}\Phi(x, y) &= e^{jk_0[\Delta_w(x,y)+\mu\Delta_l(x,y)]} \\ &= e^{jk_0\Delta_0} e^{-jk_0 \frac{x^2+y^2}{R}(1-\mu)}\end{aligned} \tag{20}$$

Since $\left[\frac{1}{R_1} + \frac{1}{R_2}\right](1 - \mu) = \frac{1}{F}$ with $\mu = c_1/c_2$ and radius of curvature on either side of lens $R_1 = R_2 = R$. Phase function becomes,

$$\Phi(x, y) = e^{jk_0\Delta_0} e^{-jk_0 \frac{x^2+y^2}{2F}} \tag{21}$$

8. Appendix B

Gabor model for PA signal: The ideal PA signal from a cylindrical source is a **N** shaped pulse. Consider a frequency dependent attenuating medium and

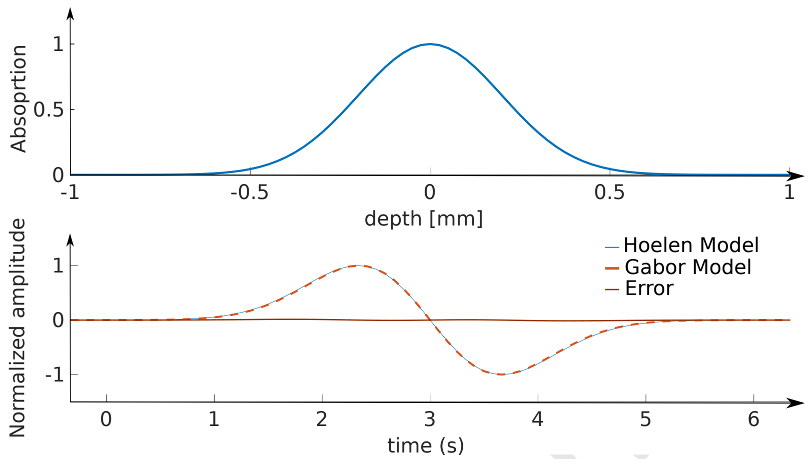

Figure 8: Gaussian absorption profile and PA signal generated using the Hoelen model [24] and with the proposed Gabor wavelet model. Error between these models are also compared.

bandlimited transducers. In most practical applications an ideal cylindrical pressure profile can be replaced with a Gaussian function,

$$A(r) = A_0 e^{-\frac{1}{2}\left(\frac{r}{R_e}\right)^2}, \tag{22}$$

where R_e is the $1/\sqrt{e}$ radius of the Gaussian function. The peak to peak time for the PA signal generated from the pressure distribution is given by,

$$\tau_{pp} = \frac{2R_e}{c}. \tag{23}$$

The corresponding PA signal proposed by Hoelen et al. [24] is

$$P(r,t) = P_{max}\frac{t-\tau}{\tau_{pp}/2}\sqrt{e}\ e^{-\frac{1}{2}\left(\frac{t-\tau}{\tau_{pp}/2}\right)^2}. \tag{24}$$

This is clearly the **N** shaped pulse modulated by Gaussian function of the source. PA signal model proposed in this work using Gabor wavelet is given by,

$$P(r,t) = P_{max} e^{-\frac{1}{2}\left[\frac{t-\tau}{\tau_{pp}/2}\right]^2} e^{-i\omega_0(t-\tau)}, \tag{25}$$

where we replace the **N** shaped pulse with a sinusoid. Fig. 8 shows a Gaussian pressure profile and we compare PA signals generated by both the models and the error signal as well. It is clear that the proposed Gabor wavelet model is almost identical to the Hoelen model.

Kalloor Joseph Francis graduated in Electronics and Communication Engineering from Calicut university in 2011. He received his master degree in Communication and Signal Processing from Christ University in 2013. He is a Fulbright-Nehru doctoral researcher at Rochester Institute of Technology. He is currently working towards his Ph.D. degree at Indian Institute of Technology, Hyderabad. His research interest lies in medical imaging. Presently, his research focus is in developing an accurate and affordable photoacoustic system for early cancer diagnosis.

Bhargava Chinni is a Master of Science graduate in Electrical Engineering from Rochester Institute of Technology, NY, USA. His primary research interests include data analytics, photoacoustic imaging, computer vision, signal and image processing.

Sumohana Channappayya received his PhD degree in ECE from the University of Texas at Austin in 2007. He is currently Associate Professor of Electrical Engineering at the Indian Institute of Technology Hyderabad. His research interests include image and video quality assessment, biomedical imaging and image processing.

Rajalakshmi Pachamuthu received her PhD degree in Electrical Engineering from the Indian Institute of Technology, Madras in 2009. She is currently Associate Professor of Electrical Engineering at the Indian Institute of Technology Hyderabad. Her research interests include Wireless Communication, Wireless Sensor Networks, Embedded Systems, Cyber Physical Systems/ Internet of Things, Green Communications, and Ultrasound Imaging.

Vikram S. Dogra, MD Professor of Radiology, Urology, and Biomedical Engineering at the University of Rochester School of Medicine in Rochester, NY as well as affiliate Professor of Imaging Science at Rochester Institute of Technology. Applications of ultrasound and Photo- acoustic imaging for clinical diagnosis and research are his main passion. His special skills include organizational capacity, leadership, and depth of clinical knowledge in applications of ultrasound and problems faced in the cancer detection.

Navalgund Rao received his Ph.D. degree in Physics from University of Minnesota in 1979. After working as a Post-doc at Ohio State University, a geophysicist at Shell Oil Company and NIH fellow at Colorado Health Science center, he has been an Imaging Science professor at Rochester Institute of Technology for the past 29 years. His research interests are in medical Ultrasound and Photoacoustic Imaging and spectroscopy and the development of new imaging technologies and image processing methodologies.